Journal of Nuclear Materials 412 (2011) 72–81

Contents lists available at ScienceDirect

Journal of Nuclear Materials

journal homepage: www.elsevier.com/locate/jnucmat

Malonic acid: A potential reagent in decontamination processes for Ni-rich alloy surfaces

D. García [a,b], V.I.E. Bruyère [a,b], R. Bordoni [a], A.M. Olmedo [a], P.J. Morando [a,b,c,*]

[a] Gerencia Química, Comisión Nacional de Energía Atómica, Centro Atómico Constituyentes, Av. Gral Paz 1499, 1650 San Martín, Prov. de Buenos Aires, República Argentina, Argentina
[b] Instituto de Tecnología, Prof. Jorge Sabato, Universidad Nacional de General San Martín, CNEA, CAC, Argentina
[c] Consejo Nacional de Investigaciones Científicas y Técnicas, Argentina

ARTICLE INFO

Article history:
Received 13 July 2010
Accepted 7 February 2011
Available online 13 February 2011

ABSTRACT

The ability of malonic acid as a dissolution agent toward synthetic Ni ferrite and Alloy 600 and 800 corrosion products was explored. Its performance in the dissolution kinetics of Ni ferrite powders was compared with the one of oxalic acid. Kinetic parameters were obtained and the dependency on external Fe(II) was modelled. Oxidized samples used in descaling tests were prepared by exposure of coupons of both alloys to lithiated aqueous solutions, under hydrothermal conditions and hydrogen overpressure, simulating PHWR conditions. Oxide layer morphology, the influence of exposure time to corrosive medium and LiOH concentration on its thickness were characterized. Descaling tests consisting on a two-stage method (a first oxidizing step with alkaline permanganate followed by a reducing step with oxalic or malonic acid were carried out).

Results were compared to those obtained with a well known chemical cleaning formulation (APAC: Alkaline Permanganate Ammonium Citrate) used in decontamination of several reactors and loops and the competitiveness of malonic acid was demonstrated.

1. Introduction

Alloy 600 and Alloy 800 are of widespread use as structural materials in different components of water-cooled nuclear reactors since more than three decades ago [1,2]. These materials normally have low average corrosion rates due to a careful control in PWR and PHWR coolants, but a measurable corrosion occurs. A remarkable characteristic of corrosion films formed on steels and these alloys under exposure to high temperature aqueous media is the formation of a duplex scale which has been extensively described in the literature [1–11]. The growth of films on the different alloys in a cooling circuit, like the primary and secondary sides of a nuclear power plant, is the result of their oxidation but also from the deposition of products generated in the medium in contact with the material itself and from the corrosion of the materials elsewhere of the cooling circuit.

Alvarez et al. [6] and Olmedo et al. [8,9] have studied oxide films grown on Alloy 800 exposed to high temperature aqueous media simulating PWR coolant conditions and have observed the formation of a double layer structure. The oxide thickness was about 150 nm for exposures of 360 and 770 h at 350 °C and it did not increase appreciably with exposure time. Conventional X-ray diffraction analyses revealed spinel structures such as magnetite, chromites and/or ferrites. EDS analyses of large crystals detached from the outer layer showed mostly iron and nickel and a very low chromium content. Stellwag [10] oxidized samples of this Alloy simulating PWR coolant conditions and reported a similar double layer structure; its thicknesses ranged between 200 and 300 nm (300 °C and 100–5000 h exposure time). The inner layer consisted of microcrystallites of a chromium-rich spinel and the outer one of larger octahedral crystals of magnetite and/or an iron–nickel spinel. The nickel content in the outer layer was variable (up to 30% in weight) and in some samples minor amounts of chromium (<5% in weight) were found.

Recent works on oxide films grown on Alloy 600 [8,12–14] under simulated PWR primary circuit conditions have also shown the build-up of a double layer structure whose characteristics depended on the dissolved hydrogen (DH) content. As an example, Terachi et al. [12] performed several autoclave tests at 320 °C for about 1000 h, varying the DH content (without DH, and at 1.0, 2.75 and 4.0 ppm DH) and observed that the oxide morphology and composition changes with DH. They found that the film grown without DH consisted of needle-like oxide and small particles, mainly composed of nickel oxide; whereas at 1 ppm DH only needle-like oxide similar to a Fe, Cr and Ni spinel oxide

* Corresponding author at: Gerencia Química, Comisión Nacional de Energía Atómica, Centro Atómico Constituyentes, Av. Gral Paz 1499, 1650 San Martín, Prov. de Buenos Aires, República Argentina, Argentina. Tel.: +54 11 6772 7176; fax: +54 11 6772 7886.
E-mail address: morando@cnea.gov.ar (P.J. Morando).

0022-3115/$ - see front matter © 2011 Elsevier B.V. All rights reserved.
doi:10.1016/j.jnucmat.2011.02.022

(Fe_x Cr_y Ni_z O_4) was observed in the outer layer. At DH >2.75 ppm, the oxide film was thinner and consisted of an outer layer of non-stoichiometric nickel ferrite particles over an inner layer of a chromite-type structure. The oxide thickness ranged from approximately 610 nm (zero DH) to 130 nm (4 ppm DH).

In several components of water cooled reactors, i.e. steam generators tubing, the continuous deposition (enhanced by temperature, crevices, thermohydraulic conditions, and so on) produces fouling (with a consequent decrease in heat transfer rates), pitting and other forms of corrosion. So it is necessary to proceed periodically to a chemical cleaning (secondary side) in order to remove the deposits and oxide layers to increase the heat transfer efficiency or to a decontamination (primary side) in order to decrease radiation fields associated to corrosion products.

Some decontamination procedures for stainless steel surfaces involve two stages: an oxidizing one for chromium oxides removal and a reducing one, in which oxalic acid has been used, in some countries, for iron oxides dissolution. However, oxalic acid is rather aggressive to the base metal; in particular it has been reported intergranular attack to stainless steel [15] exposed to it. Moreover, a well known decontamination procedure AP-CITROX, that has been used quite extensively [4,16–18] is not suitable for Alloy 600 since it produces a higher corrosion to the base material as compared to other decontamination procedures. Varga et al. [19] have documented that the chemical decontamination carried out by a version of AP-CITROX exerts a detrimental effect on the corrosion resistance of steel surfaces on the long run.

On the other hand, the results of basic studies on dissolution mechanisms of powdered Ni ferrites and Ni oxides [20,21] suggest the possible dissolution of oxides grown over Ni-rich alloys by action of oxalic acid solutions in milder conditions (less than 5% H_2Ox an lower temperatures) than those used in AP-CITROX procedure. In addition, our group has previously studied the interaction of iron oxides and malonic acid [15] and has proven its potentiality as a chemical cleaning reagent for corroded stainless steel surfaces.

This work describes the effectiveness of malonic acid for dissolution of powdered nickel ferrite and oxides grown on Alloy 600 and Alloy 800, in hydrothermal conditions. Dissolution kinetics were modelled and optimum process variables (pH, external ferrous ion concentration) were defined from experimental data on synthetic oxides. Oxidized samples of Alloy 600 and 800 were prepared by exposure of coupons to lithiated water, under hydrothermal conditions and hydrogen overpressure, simulating PHWR conditions. Oxide layer morphology and the influence of exposure time and LiOH concentration on its thickness were characterized. Several cleaning solutions were tested on oxidized and blank coupons. Their effectiveness is discussed.

2. Materials and methods

2.1. Reagents

Tridistilled water from a quartz apparatus and analytical grade reagents were used for all experiments, unless otherwise specified.

2.2. Materials

2.2.1. Ni ferrite powders

Ni ferrites were synthesized according to a coprecipitation method developed by Tamura and Matijević [22], slightly modified in our laboratories [23,24]. Samples were prepared for elemental analyses by dissolution in hot hydrochloric acid. Iron content was determined spectrophotometrically in a HP8453 diode – array spectrophotometer using thioglycollic acid as a reagent [25]. Ni content was determined by atomic absorption spectrometry in a Perkin Elmer A Analyst 100 spectrometer. Morphology and particle size were characterized using a Philips SEM 515 microscope. X-ray diffractograms of powdered samples were obtained using Cu Kα radiation in a Siemens D-5000 diffractometer equipped with a graphite monochromator. Specific surface areas of powdered ferrites were obtained in a Micromeritics Accusorb 2100D using N_2 as an adsorbate and BET isotherm.

2.2.2. Metallic coupons

2.2.2.1. Blank coupons. Nuclear grade Alloy 800 machined from original Embalse Nuclear Power Plant steam generator tubing and two batches of Alloy 600 samples provided by KWU (in 1983), one in plate shape and another in tube shape, were cut to obtain coupons which characteristics are shown in Table 1.

The surfaces of most samples were mechanically abraded with silicon carbide papers down to 1000 grit. Alloy 600 tube samples were polished with silicon carbide papers down to 600 grit. Alloy 600 tube samples, used to grow the thickest oxide films (around 2 μm) were tested in the as received surface condition. After polishing, all samples were thoroughly degreased with acetone and cleaned with tridistilled water, acetone, stored for at least 24 h in a dessicator over silica-gel and then coated with a thin gold film (ca. 30 nm) before SEM examination.

2.2.2.2. Oxidized coupons. Thin oxide layers were grown on a set of blank coupons over a 20 days period in static stainless steel conditioned autoclaves at 350 °C. Hydrogen overpressure of approximately 98 kN m^{-2} and 4×10^{-4} mol dm^{-3} aqueous LiOH (pH 25 °C ≅ 10.4), were used.

Thick oxide layers (around 2 μm) were grown over a period of 4 days in the same autoclaves (with a previously oxidized stainless steel liner) and other conditions as mentioned above except for the aqueous phase, consisting on 0.6 mol dm^{-3} LiOH.

The morphology of the oxide layers and the surface of the descaled samples and blank coupons were examined by SEM, using a Philips SEM 515 microscope. The elemental composition was determined by X-ray energy dispersive spectroscopy (EDS). Some films were analyzed by conventional X-ray diffraction (XRD) with a Philips PW3710 diffractometer and at grazing incidence with a Siemens D-500 diffractometer. The instruments were equipped with monochromator and Cu Kα radiation was used in both cases. The elemental composition of the thicker oxide films was determined in cross section with EDS at different positions from the oxide–metal interface.

Table 1
Coupons' composition and size.

Alloy	Weight% composition									Size (length × width × thickness)/cm
	Fe	Ni	Cr	Mn	Ti	C	Co	Cu	Si	
800[a]	Balance	32.50	20.50	0.75	0.44	0.022	0.01	0.07	n.d.	5.0 × 1.0 × 0.18
600[b]	8.50	74.7	16.5	0.75	–	0.04	–	0.07	n.d.	5.0 × 2.5 × 0.10
600[c]	8.37	76.10	15.00	0.16	–	0.03	–	0.05	0.26	3.0 × 1.25 (outer diam.) × 0.12

n.d.: not determined.
[a] Quarter tube shape.
[b] Plate shape.
[c] Half tube shape.

3. Experimental

3.1. Oxide dissolution experiments

3.1.1. Synthetic oxides

A thermostated (±0.1 °C) glass double jacketed cell with a PTFE stopper was used in dissolution experiments. The suspension was magnetically stirred and deareated through purified N_2 bubbling; T (70.0 °C) and pH were continuously monitored. Reactions were carried out in the dark (the cell was wrapped in two sheets of aluminum foil), aliquots were withdrawn periodically by means of a micropipet, immediately filtered through 0.22 μm cellulose acetate membranes and diluted conveniently. Iron and/or nickel content were determined by visible spectrophotometry and atomic absorption spectrometry respectively, as described above.

In a typical run ca. 20 mg of powdered Ni ferrite were poured at $t = 0$ in a thermostated, deareated, magnetically stirred liquid phase consisting on 100 mL of a solution of the acid under study at desired concentration and pH. In all cases ionic strength was adjusted to 0.500 mol dm^{-3} with $NaClO_4{\cdot}H_2O$. In those cases where Fe(II) influence was studied, it was added as solid $Fe(NH_4)_2(SO_4)_2{\cdot}6H_2O$ (Mohr's salt) 10 min before oxide addition.

3.1.2. Coupon descaling tests

A two-stage method was used: first an oxidizing treatment (alkaline permanganate) and then a reductive process with malonic acid (or oxalic or citric acid).

Descaling experiments were conducted in the same glass cell used for powder oxide tests and consisted on suspending oxidized and not exposed to oxidation ("blanks") coupons and totally immersing them in the descaling solutions. During descaling, the solutions were continuously stirred and the cell was wrapped in two sheets of aluminum foil. The solution's composition and operative conditions are shown in Table 2. After descaling, all specimens were thoroughly cleaned in an ultrasonic bath with tridistilled water, washed in ethyl alcohol, acetone, air-dried and stored in a vacuum dessicator for at least 10 h before weighing. Experimental results are presented as the average of 3 tests on different coupons.

A well known method [4,16,26] was used in order to calculate corrosion and oxide thickness. The coupons were weighed (1) before exposure in the autoclave, (2) after exposure, (3) after ultrasonic cleaning and (4) after chemical descaling. Blanks were treated similarly to provide an estimate of the base metal general corrosion or attack (if any). Total corrosion was calculated as the difference between the weight of the coupon before and after descaling, corrected for the bare coupon (blank) corrosion. The areas of the oxidized and bare coupons were taken into account in the calculations to obtain the oxide thickness and corrosion, expressed as weight loss per unit area. The density of magnetite, iron chromites and nickel ferrites are similar and a value of 5.2 g cm^{-3} was used to estimate the oxide thickness.

Table 2
Description of different procedures used in descaling. All reactions were carried out at 90 °C.

Procedure	Stage	Composition	Concentration (weight%)	pH	Contact time (h)
APMAL	Oxidizing	$KMnO_4$	3.0		1
		NaOH	10.0		
	Reducing	$H_4C_3O_4$	10.0		
		Fe(II)	5.5×10^{-4} mol dm^{-3}	4.5	1
APOX	Oxidizing	$KMnO_4$	3.0		1
		NaOH	10.0		
	Reducing	$H_2C_2O_4$	6.3	3.5	1
APAC	Oxidizing	$KMnO_4$	3.0		1
		NaOH	10.0		
	Reducing	$(NH_4)_2HC_6H_5O_7$	10.0	4.7	1

4. Results and discussion

4.1. Ni ferrite powder assays

4.1.1. Oxide characterization

Elemental analyses results gave Fe/Ni molar ratios that were slightly higher than stoichiometric ones, resulting in a formula $Ni_{0.99}Fe_{2.03}O_4$. Deviations from stoichiometry were previously reported [23,24] and attributed to the presence of hematite as a separated phase. This fact was confirmed by X-ray diffraction. The addition of hematite as an internal standard to synthetic Ni ferrite samples let estimate 5% as an upper limit for hematite content in those samples, as calculated through X-ray diffraction data and according to chemical analyses. This hematite is present as a surface layer [20] and was eliminated before kinetic studies (see Section 4.1.2.1). A SEM micrograph of synthetic Ni ferrite powder is shown in Fig. 1. The average particle size was ca. 0.2 μm. BET surface area was 17.5 m^2 g^{-1}.

4.1.2. Dissolution mechanisms

4.1.2.1. Comparison of Ni ferrite dissolution by oxalic and malonic acid. A previous study on oxalic acid dissolution of Ni ferrites [20] was carried out without light protection. Since it was demonstrated that light photocatalyzes this reaction [24,27] and in order to avoid its influence, all dissolution assays were done in the dark. Fig. 2 represents several dissolution profiles for a synthetic Ni ferrite in different media containing oxalic and malonic acid. Dissolution fraction f is defined as:

$$f = \frac{\omega_o - \omega}{\omega_o}, \tag{1}$$

where ω_o is the initial ($t = 0$) oxide mass and ω is the oxide mass remaining at a given arbitrary reaction time t.

If the oxide is a mixture of two different phases, both dissolution processes may take place at different rates, thus being time-resolved. This is the case for oxalic [23,24] and malonic (this work) acid dissolution of hematite-containing Ni ferrite: superficial hematite dissolves first, then Ni ferrite dissolution takes place. It is of interest to focus on ferrite dissolution. There are two ways of taking this fact into account: (i) dissolution curves can be time-normalized; or (ii) a previous acid attack can be done, then a ferrite dissolving step can be studied independently. The next discussion refers to the dissolution of the ferrite phase, once the

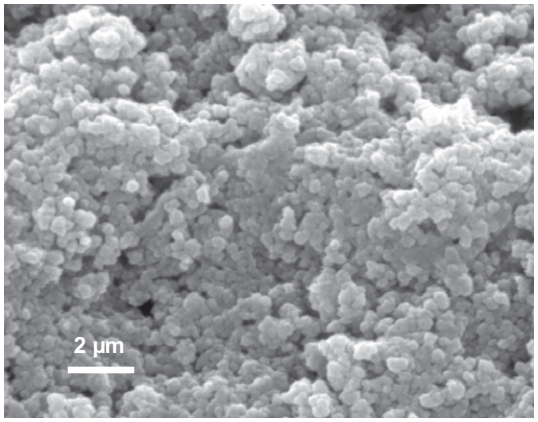

Fig. 1. SEM micrograph of synthetic Ni ferrite.

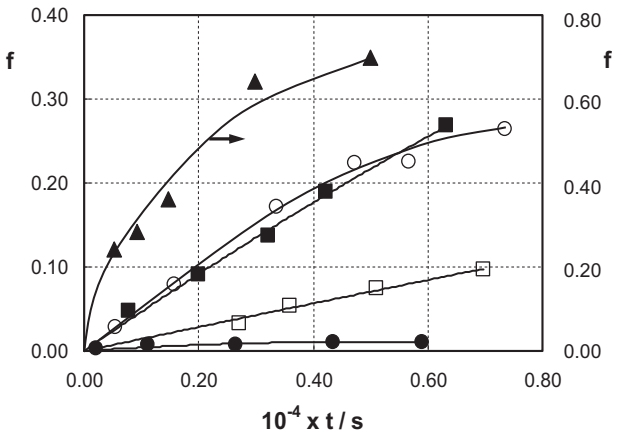

Fig. 2. Dissolution fraction (f) vs. time (t) for Ni ferrite at 70.0 °C and ionic strength ($NaClO_4{\cdot}H_2O$) = 0.5 mol dm^{-3}, in: 0.1 mol dm^{-3} oxalic acid, pH = 3.5 (□); 0.2 mol dm^{-3} oxalic acid, pH = 3.5 (■); 0.1 mol dm^{-3} oxalic acid, pH = 3.5, [Fe(II)] = 2.50 × 10^{-3} mol dm^{-3} (▲); 0.2 mol dm^{-3} malonic acid, pH 4.5 (●); 0.2 mol dm^{-3} malonic acid, pH 4.5, [Fe(II)] = 3.58 × 10^{-4} mol dm^{-3} (○).

surface hematite layer has been dissolved. Congruent dissolution of Ni ferrite was previously demonstrated for oxalic acid-containing media [24]. This was also confirmed in this work for both acids, then reaction course was monitored only through Fe release. Rate constants were obtained upon linearization of f vs. t plots through contracting sphere model [28] which leads to:

$$1(1-f)^{1/3} = k't. \tag{2}$$

Reported k′ (s^{-1}) values were obtained from the slope of $1-(1-f)^{1/3}$ vs. t plots (see Eq. (2)) through least squares method and were expressed as specific rate constants k, in mol Fe m^{-2} s^{-1}, through Eq. (3):

$$k = \frac{k' \times 2.03}{Mr \times \overline{A}}, \tag{3}$$

where 2.03 represents the Fe/oxide molar ratio, *Mr.* the relative molar mass and $\overline{A}$ is the specific surface area for Ni ferrite. Each k value resulted from the average of two independent experiments that differed in less than 5%.

Oxalic acid concentration dependency for Ni ferrite dissolution was also explored in a previous paper [20]. Experimental data were fitted according to a Langmuir-type expression:

$$k = \frac{k_{max} \times [H_2Ox]}{(K_{ads})^{-1} + [H_2Ox]}, \tag{4}$$

where k is the specific dissolution rate (mol Fe m^{-2} s^{-1}), [H_2Ox] is oxalic acid bulk (nominal) concentration (mol dm^{-3}) and k_{max} (mol Fe m^{-2} s^{-1}) and K_{ads} (mol^{-1} dm^3) are both constant in Eq. (4). The values reported in that paper were k_{max} = 1.02 × 10^{-7} mol Fe m^{-2} s^{-1} and K_{ads} = 20.8 mol^{-1} dm^3 (70.0 °C).

In the malonic acid case, dissolution rates of nickel ferrites are very low in the absence of added Fe(II) ion (less than 5% dissolution for 5 h reaction time in 0.2 mol dm^{-3} malonic acid at 70.0 °C and pH 4.5. Thus, in order to achieve measurable reaction rates, experiments with malonic acid were carried out in the presence of different amounts of added Fe(II) (see Section 4.1.2.2). Data processing was similar for oxalic and malonic acid as solvents and contracting sphere model was suitable in both cases.

In the surface complexation model, the first step in oxide dissolution is an adsorption of solvent on oxide surface [28]. Specifically, in the case of iron oxides it is widely demonstrated that Fe(II) ions are more labile than Fe(III) ions [28]. For this reason, the presence of Fe(III)-reducing agents in dissolving media results in an enhancement in dissolution rate for Fe(III)-containing oxides.

Ni ferrite dissolution mechanism in the presence of aqueous oxalic acid was described previously [20] and implies the occurrence of two parallel pathways: acid-assisted dissolution and reductive dissolution. An initial proton and HOx^- attack to the oxide leads to the formation of a surface oxalate complex (represented as ≡Fe(III)—OxH in equation:

$$\equiv Fe(III)—OH + H^+ + HOx^- \leftrightarrows \equiv Fe(III)—OxH + H_2O, \tag{5}$$

and starts the sequence of reactions that give rise to dissolution.

Phase transfer may be accounted for by an acid-assisted dissolution (releasing complex Fe(III) ions that are subsequently reduced to complex Fe(II) ions in the aqueous phase, Eqs. (6) and (7):

$$\equiv Fe(III)—OxH \overset{HOx^-,H^+}{\rightarrow} \equiv OH + \left[Fe(III)(HOx)_n\right]_{(aq)}^{(3-n)+}, \tag{6}$$

$$\left[Fe(III)(HOx)_n\right]_{(aq)}^{(3-n)+} + (m-n+1)HOx^- \rightarrow [Fe(II)(HOx)m]_{(aq)}^{(2-m)+} + HOx^{\cdot}, \tag{7}$$

or by direct reduction of surface Fe(III) ions (where an intermediate species ≡Fe(II)—$HOx^{\cdot-}$ probably forms) through Eq. (8), thus releasing Fe(II) ions:

$$\equiv Fe(III)—OxH \overset{HOx^-,H^+}{\rightarrow} \equiv OH + \left[Fe(II)(HOx)_m\right]^{(2-n)+}(aq) + HOx^{\cdot}. \tag{8}$$

In both cases, the net result is the aqueous phase becoming enriched in Fe(II) complexes that can be adsorbed onto the oxide surface, thus leading to more dissolution events through a reductive mechanism. Eqs. 9, 9′, 10, 10′, 11, 11′ (where charges are omitted for simplicity) show its different steps: (i) the intervalence complex (Eq. (9)) or ionic pair association (Eq. (9′)) formation, (ii) the inner sphere (Eq. (10)) or outer sphere (Eq. (10′)) electron transfer; and (iii) the phase transfer processes (Eqs. (11) and (11′)):

$$\equiv Fe(III)—OxH + \left[Fe(II)(HOx)_n\right]_{(aq)} \rightarrow \equiv Fe(III)—Ox—Fe(II)(HOx)_m + HOx^-, \tag{9}$$

$$\equiv Fe(III)—HOx + \left[Fe(II)(HOx)_n\right]_{(aq)} \rightarrow \equiv Fe(III)—HOx\cdots Fe(II)(HOx)_n, \tag{9′}$$

$$\equiv Fe(III)—Ox—Fe(II)(HOx)_m \rightarrow \equiv Fe(II)—Ox—Fe(III)(HOx)_m, \tag{10}$$

$$\equiv Fe(III)—HOx\cdots Fe(II)(HOx)_n \rightarrow \equiv Fe(II)—HOx\cdots Fe(III)(HOx)_n, \tag{10′}$$

$$\equiv Fe(II)—Ox—Fe(III)(HOx)_m \overset{HOx^-,H^+}{\rightarrow} \equiv OH + \left[Fe(II)(HOx)_n\right]_{(aq)} + [Fe(III)(HOx)_n]_{(aq)}, \tag{11}$$

$$\equiv Fe(II)—Ox\cdots Fe(III)(HOx)_m \overset{HOx^-,H^+}{\rightarrow} \equiv OH + \left[Fe(II)(HOx)_n\right]_{(aq)} + \left[Fe(III)(HOx)_n\right]_{(aq)}, \tag{11′}$$

where ≡OH represents a surface —OH group: ≡Fe(III)—OH.

The Fe(III) aqueous complex produced in Eqs. (11) and (11′) is further reduced through Eq. (7).

Although oxalic acid is more reactive than malonic acid toward Ni ferrite dissolution, the mechanism is quite similar for both acids, as it is evidenced through dissolution factor (f) vs. time profiles and Fe(II) dependence (see Section 4.1.2.2). Thus, Eqs. (5)–(11′) are suitable for the interpretation of dissolution processes in both cases. The possible dissolution mechanisms are summarized in Fig. 3, where oxalic acid behavior is exemplified. The dual character

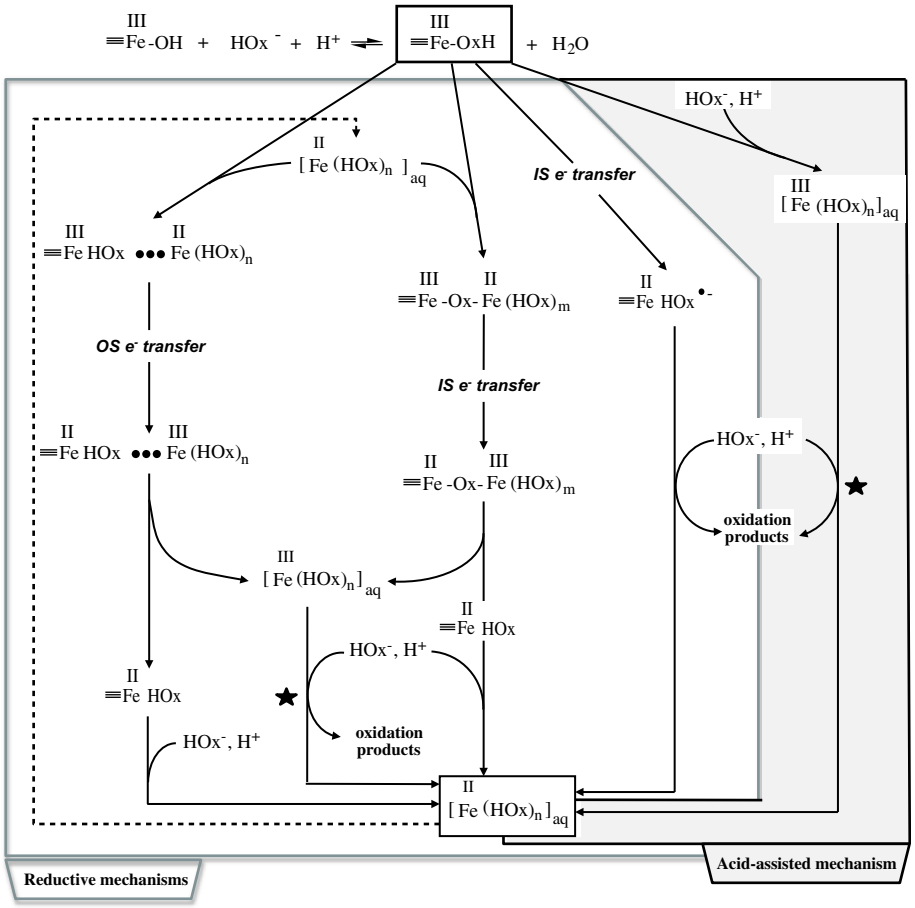

Fig. 3. Dissolution mechanisms of iron(III)-containing oxides in oxalic acid media. Surface —OH groups and some charges were omitted for simplicity. ★ Note that these steps are common to both mechanisms. - - - - autocatalytic feedback.

of reducing and/or complexing agent of oxalic and malonic acid makes possible the coexistence of both dissolution mechanisms (i.e. acid-assisted and reductive dissolution).

In the case of oxalic acid, the preeminence of the reductive over acid-assisted mechanism at $T \geqslant 70$ °C was suggested [29].

4.1.2.2. External Fe(II) influence. The catalytic effect of Fe(II) ion on the dissolution of nickel ferrite by both acids is illustrated in Fig. 2. It can be seen that dissolution percentages close to 25% are achieved in 100 min for [Fe(II)] = 3.58×10^{-4} mol dm^{-3}, [Mal] = 0.2 mol dm^{-3} and pH = 4.5. In spite of being lower than that reached in the presence of oxalic acid in similar conditions, this value let us think of malonic acid as an effective decontamination agent (or chemical cleaning agent) in the presence of aqueous Fe(II).

Dependency of dissolution rate constants on external Fe(II) concentration in 0.2 mol dm^{-3} malonic acid (Fig. 4) can be adjusted to a Langmuir-type isotherm (similar to Eq. (4)) which parameters are: $k_{max} = 1.87 \times 10^{-8}$ mol Fe m^{-2} s^{-1} and $K_{ads} = 2.9 \times 10^3$ mol^{-1} dm^3.

According to this fitting, maximum rates are achieved at [Fe(II)] $\geqslant 5 \times 10^{-3}$ mol dm^3. However, these values cannot be extrapolated directly to a practical use of malonic acid as chemical cleaning or decontamination agent for corroded metal surfaces. During these procedures ferrous ions, among others, build up (local accumulation of ions) close to those surfaces leading to (undesirable) precipitation, under certain conditions, of some iron-containing phase or phases. The amount of Fe(II) to be used in order to achieve a good performance of the cleaning solution must arise from a balance between catalytic effect on one hand, and local precipitation and waste generation, on the other hand. It has to be noted here that the figures obtained with powdered oxides are useful in order to make a choice among several possible reagents but tests on representative samples not only of the oxide involved but also on the surface to be cleaned (decontaminated) must also be carried out.

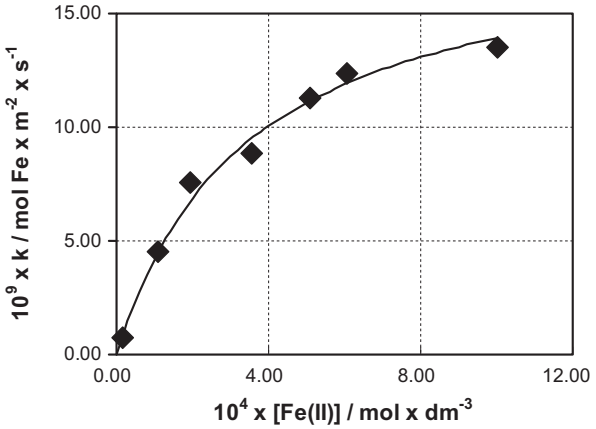

Fig. 4. Ni ferrite dissolution rate constant (k) dependency on Fe(II) concentration in 0.200 mol dm^{-3} malonic acid at pH = 4.5 and ionic strength = 0.500 mol dm^{-3} ($NaClO_4$·H_2O). Solid line represents fitting according to a Langmuir-type expression similar to Eq. (4).

4.1.2.3. pH dependency. The plots of ferrite dissolution rate constant vs. pH, in malonic acid media containing Fe(II), show a bell-shaped curve. This fact was previously reported in bibliography for weak acid dissolution of transition metal oxides [15,30,31]. The shape of these curves was interpreted as the balance of two pH-dependent opposing factors: (a) the surface protonation and (b) the concentration of anionic species of the weak acid. As pH rises, surface protonation becomes less important, leading to lower dissolution rates. On the other hand, the concentration of anionic species of the weak acid rises as pH values become higher. Since one or more of these species are usually the reactive species, this effect would contribute to an increase in the reaction rate. The net result is a maximum in dissolution rate at a certain intermediate pH value. The optimum pH value obtained in this work for malonic acid dissolution of Ni ferrite was 4.5, and it was previously found to be 3.5 in the case of oxalic acid dissolution of Ni ferrite [32]. This is a good point for malonic acid as decontaminant (or chemical cleaner) reagent, since more acidic conditions enhance corrosion tendency.

4.2. Coupon tests

4.2.1. Oxide layers grown under hydrothermal conditions

The corrosion of the Fe–Cr–Ni alloys tested in this work under PHWR hydrothermal conditions can be described by parabolic or logarithmic kinetics, so corrosion rates are high at initial exposures during the buildup of the protective oxide film and then decrease to steady-state levels [6,9,33–35], in such a way that its thickness do not increase appreciably with additional exposure time.

4.2.1.1. Alloy 800. SEM micrographs of the oxide grown 20 d at 350 °C over Alloy 800 are shown in Fig. 5. In agreement with earlier works [6,8–10] the oxide double layer is observed: a non-compact layer of octahedral or polyhedral crystals of different size over a smooth and compact layer of very tiny crystallites.

Conventional X-ray diffraction analysis showed sharp and distinct peaks of the underlying base metal and small and broad peaks of the oxide. Five of the more intense peaks of spinel structures were identified and assigned to $FeCr_2O_4$, $(Ni,Fe)Fe_2O_4$, $NiCr_2O_4$ and/or Fe_3O_4. Grazing incidence X-ray diffraction data (not shown) exhibited broad oxide signals, due to an evident peak overlapping, thus the presence of $NiCr_2O_4$, $FeCr_2O_4$, $(Ni,Fe)Fe_2O_4$ and Fe_3O_4, was inferred. Due to the thinness of the oxide layer and the grazing incidence angle used, base metal reflections were also very strong as compared to oxide film reflections. Composition differences between inner and outer layer cannot be distinguished using this technique due to the area scanned by the X-ray beam and the thinness of the oxide layer, thus showing the species present in both layers [8,9].

Fig. 6a shows the oxide morphology of the thicker oxides grown in aqueous [LiOH] $\approx$ 0.6 mol dm^{-3}. The outer layer of the film is composed of two families of crystals: one consisting on a compact arrangement of crystals ranging 0.5–1 μm and the other of larger crystals (2–5 μm).

The oxide thickness can be estimated in about 2 μm (Fig. 6b). The elemental composition analyses by EDS of the central crystal (see arrow) in Fig. 6a were (in weight%): 87.2% Fe, 8.8% Ni, 3.4% Cr; the analyses of other large crystals gave similar results, indicating Fe enrichment (see Table 1).

Fig. 7 shows the elemental composition profile and the Cr/Ni ratio obtained by EDS through the oxide thickness of a sample oxidized 4 days at 350 °C in aqueous [LiOH] $\approx$ 0.6 mol dm^{-3}. A chromium enrichment (Cr/Ni ratio) was observed at the oxide/metal interface and an iron enrichment at the oxide/environment interface. The EDS mappings of this sample had also shown an iron enrichment at the oxide/environment interface especially in the octahedral or polyhedral crystals observed in the cross-section sample.

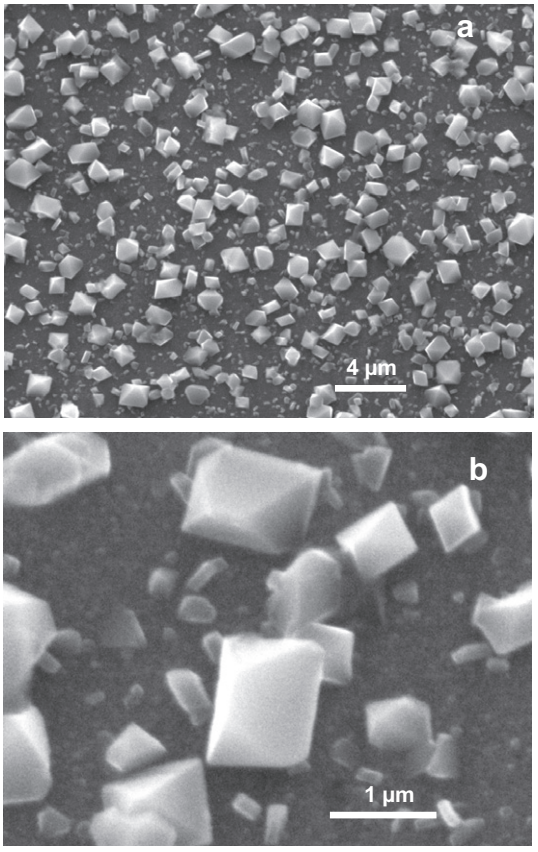

Fig. 5. SEM micrographs of the oxide layer grown on corroded coupons of Alloy 800 exposed to aqueous LiOH (pH 25 °C ≅ 10.4) for 20 d at 350 °C.

4.2.1.2. Alloy 600. Fig. 8a shows high magnification micrographs of Alloy 600 oxidized sheet samples after exposure to hydrothermal conditions during 20 days at 350 °C in aqueous LiOH (pH 25 °C ≅ 10.4). The morphology of a duplex film is clearly seen. A compact, protective film extends all over the surface beneath an external layer composed of crystallites of different sizes, some of them of octahedral morphology. According to Ziemniak and Hanson [13] the outer layer is identified as a non-stoichiometric ferrite–rich layer with a composition $(Ni_{0.9}\ Fe_{0.1})(Fe_{0.85}\ Cr_{0.15})_2O_4$ and the inner one as a chromite-rich layer.

These micrographs also show that the crystals in the outer layer are smaller than those reported previously (see Fig. 5) for the oxidized Alloy 800 samples at the same conditions and that the density (number of crystals per unit area) of the larger crystals dispersed on top of the inner layer is also lower than that observed for Alloy 800. The same analyses reported for Alloy 800 sample have been performed on a sheet sample of Alloy 600 using grazing incidence X-ray diffraction. All peaks measured correspond to a spinel oxide. The same considerations reported previously for the films grown on Alloy 800 are valid for Alloy 600 due to the thinness also observed for the oxide layers grown on it. The XRD signals of the oxide peaks are also broad. However, a careful analysis of one of the peaks indicated that the spinel oxide was dominated by the presence of a nickel ferrite ($NiFe_2O_4$), nickel chromite ($NiCr_2O_4$), and a minor amount of iron chromite ($FeCr_2O_4$) and magnetite (Fe_3O_4) [8,9].

Fig. 8b shows the oxide film grown on the tube samples at the same hydrothermal conditions that Fig. 8a. The oxide layer is similar to that grown on sheet samples, octahedral crystals are clearly

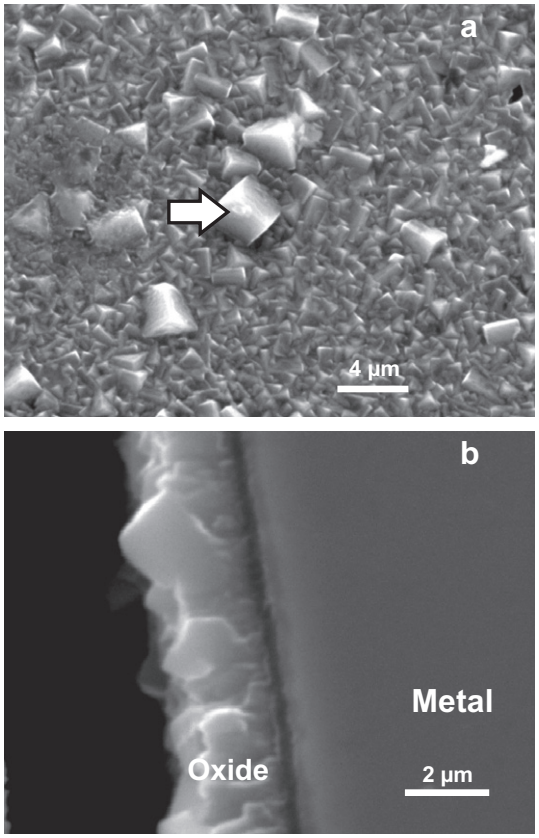

Fig. 6. SEM micrographs of the oxide layer grown on Alloy 800 coupons exposed to aqueous LiOH 0.6 mol dm^{-3} for 4 d at 350 °C, (a) and a cross section of the same oxidized coupons. (b) The arrow in (a) shows one of the largest crystals, embedded in the first oxide layer, which was subjected to EDS analyses (see Section 4.2.1.1).

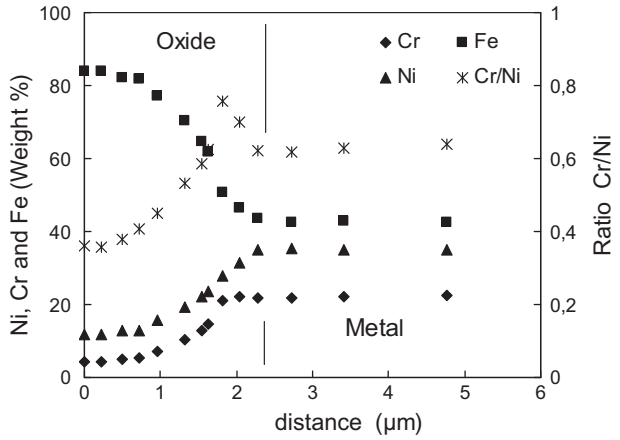

Fig. 7. Elemental composition profiles of the oxide grown over Alloy 800 coupons exposed to aqueous 0.6 mol dm^{-3} LiOH for 4 d at 350 °C.

seen dispersed over the inner layer. The grinding marks left on the surface by the preparation process are also evident.

4.2.2. Descaling tests

The reason for using a two-stage method is well documented in the literature (4). In the first stage the oxidizing reagent (AP) oxidizes Cr(III), present in the chromium rich layer grown on the surfaces of stainless steel and these alloys, to Cr(VI). The soluble species thus formed leaches out of the oxide, causing the oxide film to become porous. The residual chromium-depleted oxide (rich in

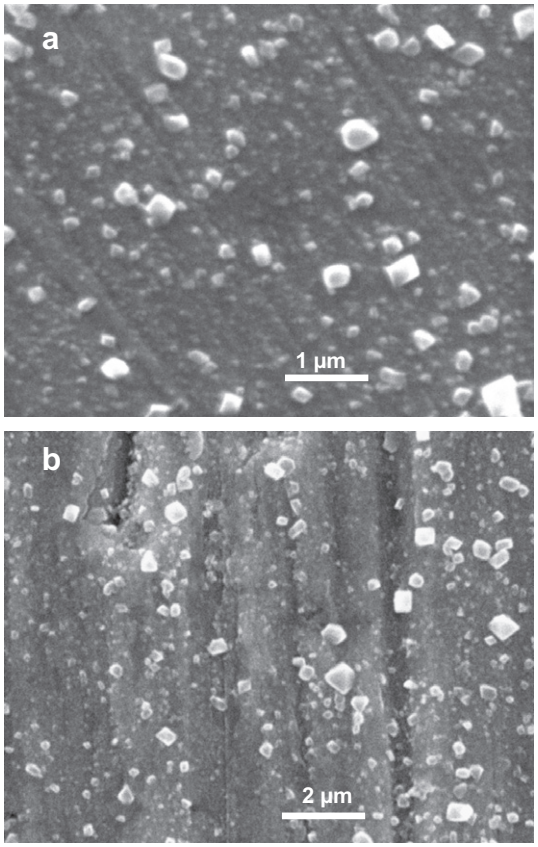

Fig. 8. SEM micrographs of Alloy 600 samples exposed to aqueous LiOH (pH 25 °C ≅ 10.4) for 20 d at 350 °C. (a) Sheet, (b) tube-shaped samples.

Fe(III)) can be then dissolved, in the second stage, under reducing conditions. In our comparative study the first stage is common for all three procedures and different carboxylic acids are used in the second stage. The results obtained for each oxidized sample are discussed in separate form.

4.2.2.1. Alloy 800.

4.2.2.1.1. Thin oxides. Table 3 summarizes experimental information for all three procedures expressed as weight loss per unit area, of oxidized and blank coupons; d_{ox} (adherent oxide) and d_{tot} (total oxide) for oxidized coupons. In all cases, the correction for base metal losses during oxide removal was done. d_{ox} is the adherent oxide thickness of the sample after oxidation and before descaling and d_{tot} is the total oxide thickness that would be generated by the coupon itself (that is, the corrosion penetration of the coupon, then converted to oxide). In this hydrothermal environment, there may be corrosion products released not only by the samples tested but also from the autoclave walls where the samples were oxidized. This means that higher values of d_{ox} as compared to d_{tot} for a specimen indicate that part of the oxide present in its surface

Table 3
Weight loss per unit area of descaled Alloy 800 coupons: adherent (d_{ox}) and total oxide (d_{tot}) components, see text.

	Corroded coupons			Blank coupons
Procedure	Weight loss (mg dm^{-2})	d_{ox} (μm)	d_{tot} (μm)	Weight loss (mg dm^{-2})
APAC	7.9	0.15	0.12	0.5
APMAL	6.8	0.13	0.15	0.7
APOX	32.2	0.62	–	0.8

was generated by corrosion of the sample itself but the overall growth of the film also involved deposition from the supersaturated solution.

It can be seen that the weight loss per unit area and the oxide thickness are similar using either APAC or APMAL methods and are in agreement with the values reported in literature for the oxide grown on Alloy 800 in similar environmental conditions [6,8–10]. The much greater weight loss determined for APOX suggests that APOX has dissolved an important mass of base material and also that the value of 0.62 μm for oxide thickness is overestimated.

Typical SEM images of the descaled surfaces using the three procedures are shown in Fig. 9.

The surface of the sample treated with APOX, Fig. 9c, reveals an extensive dissolution on several grains and pitting. This fact explains the greater weight loss of these samples as compared to those treated with APMAL and APAC (Fig. 9a and b, respectively), that had not experienced any similar corrosion attack. This fact could be explained considering a redox dissolution mechanism involving Fe^{o} from base metal acting as a reducing agent [36]. An example of such a global reaction involving magnetite would be:

$$Fe(s) + Fe_3O_4(s) + 8H^+(aq) \rightarrow 4Fe^{2+}(aq) + 4H_2O(l). \quad (12)$$

Fe(II) ions thus generated increase the aggressiveness of oxalic acid. Moreover, since reaction (12) is favored at acidic pHs, oxalic acid (optimal pH = 3.5) is expected to be more aggressive than malonic acid (optimal pH = 4.5) in descaling tests.

SEM examination of the blank descaled coupons has shown no localized attack for any of the three procedures and a weight loss per unit area <1 mg dm^{-2} was measured. This value is a typical value for the APAC procedure used on stainless steels and Alloy 800 [5,6,10]. The low value obtained for APOX procedure means that the oxide affects (through Eq. (12)) the base metal dissolution of the oxidized sample. Therefore, these results indicate that APMAL may be used as a descaling procedure since its effectiveness and base-metal corrosion are similar to APAC, while APOX must be discarded.

4.2.2.1.2. Thick oxides. Descaling tests on these oxides showed that APMAL procedure produced a weight loss around three times greater than APAC (109.1 versus 42.6 mg dm^{-2}). The thickness calculated from the weight loss using APMAL (2 μm) was similar to that obtained by SEM from the image of the metallographic cross section of a sample (Fig. 6b). No localized attack was observed in both cases.

Fig. 10 shows representative SEM micrographs of the inner surfaces of the tube samples after descaling procedures. The morphology of the sample treated with APAC shows clearly the octahedral crystals on the outer layer, suggesting a low dissolution rate for the oxide. A quite different image is seen on the surface after APMAL descaling, since nearly all the film was removed. These observations are, in both cases, in agreement with the weight loss obtained. These results indicate that APMAL is more effective than APAC for the removal of thick oxides.

4.2.2.2. Alloy 600.

4.2.2.2.1. Sheet samples. Table 4 summarizes weight loss per unit area, d_{ox} and d_{tot} for the three procedures tested. The last column represents the weight loss per unit area of blank samples. In all cases, the correction for base metal losses during oxide removal was applied. This means that the weight loss measured after descaling is the weight loss reported in the second column in Table 4 plus the weight loss of the blank coupons (column 5 in this Table). It is clear from these data that APOX treatment produces a greater blank weight loss than the other two treatments. This fact shows the importance of the correction, in order to calculate the actual values of d_{ox} and d_{tot} that are shown in columns 3 and 4 in Table 4.

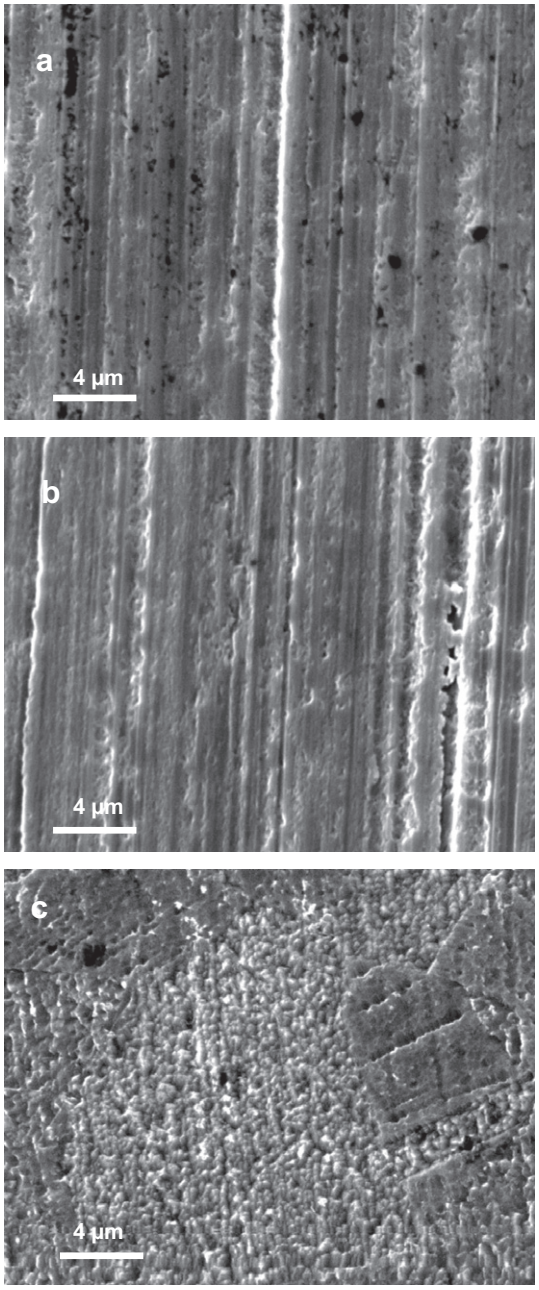

Fig. 9. SEM micrographs of Alloy 800 coupons' surfaces treated with (a) APAC, (b) APMAL, (c) APOX. See experimental details in Table 2.

The adherent oxide is similar to that reported in the literature [12–14]. In all three cases d_{tot} is slightly greater than d_{ox}, so it can be inferred that there was some release of corrosion products to the environment. The APAC treatment produced a weight loss per unit area that is similar to that reported in literature for this procedure applied to high Ni content alloys [6,7–10], but the APOX treatment produced a weight loss that is much greater than the value obtained with APAC. The APMAL treatment produced a weight loss that is somewhat larger than that obtained with APAC, but did not produce the corrosion attack reported for APOX (see Fig. 10).

Fig. 11 shows SEM micrographs of the samples after descaling. Small pits, associated with the material inclusions are seen in some zones of the sample when APOX procedure was used. The SEM observation of the blanks after descaling has shown no localized

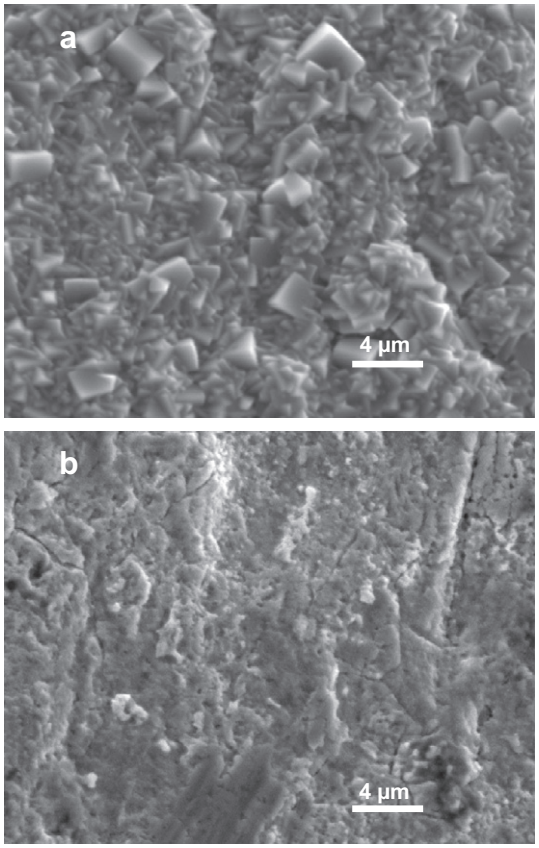

Fig. 10. SEM micrographs of the inner surface of Alloy 800 coupons descaled with (a) APAC, (b) APMAL. See experimental details in Table 2.

Table 4
Weight loss per unit area of descaled Alloy 600 sheet coupons: adherent (d_{ox}) and total oxide (d_{tot}) components, see text.

Procedure	Corroded coupons			Blank coupons
	Weight loss (mg dm^{-2})	d_{ox} (μm)	d_{tot} (μm)	Weight loss (mg dm^{-2})
APAC	6.3	0.12	0.13	0.8
APMAL	7.4	0.14	0.16	3.2
APOX	6.6	0.13	0.14	9.5

attack when APAC and APMAL were used, while the blank sample treated with APOX has shown not only some small pitting but also a greater roughness of the surface. These observations and the weight loss per unit area for oxidized coupons represent an advantage of APMAL as compared to APOX.

4.2.2.2.2. Tube samples. Table 5 summarizes the results obtained for APAC and APMAL on samples machined from Alloy 600 tubing. The values are similar for both procedures. The oxide thicknesses are larger than those obtained with the sheet samples. This fact can be related to the different surface finish of the sheet and tube samples but also to the different batches of both types of samples. It is well documented in the literature that a better surface finish generally improves the corrosion resistance, since the initial metal release is lower and the quality of the oxide film is higher [5,6,10,37]. Lister et al., performing some particular tests on SS 304 [5], reported that once a protective film is established the nucleation of the outer layer is suppressed and also found that the outer oxide layer is not protective. Guinard et al. [37] reported not only the influence of surface finishing in the corrosion rate of Alloy 600, but also that there is a clear relationship between the surface condition and the release of corrosion products. In both cases d_{tot} was slightly greater than d_{ox}, indicating there was some oxide release to the environment.

SEM examination of blank coupons after descaling (not shown) exhibited no localized attack.

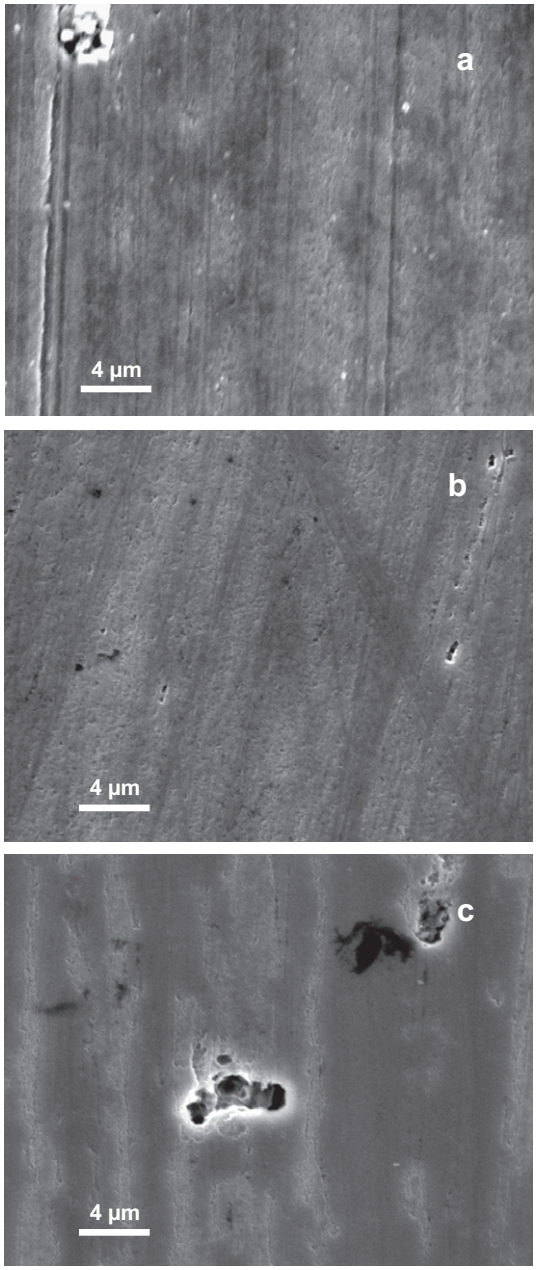

Fig. 11. SEM micrographs of the surfaces of Alloy 600 coupons descaled with (a) APAC, (b) APMAL, (c) APOX. See experimental details in Table 2.

Table 5
Weight loss per unit area of descaled Alloy 600 tube coupons: adherent (d_{ox}) and total oxide (d_{tot}) components, see text.

Procedure	Corroded coupons			Blank coupons
	Weight loss (mg dm^{-2})	d_{ox} (μm)	d_{tot} (μm)	Weight loss (mg dm^{-2})
APAC	11.2	0.22	0.27	0.2
APMAL	9.9	0.19	0.23	0.6

5. Conclusions

5.1. Powder oxides

- Synthetic Ni ferrite dissolution kinetics in the presence of malonic acid and Fe(II) was modelled according to a reductive mechanism that implies:
  - Adsorption on the surface, according to a Langmuir-type isotherm, of Fe(II) species and formation of an intervalence complex.
  - Electron transfer between its metallic centers.
  - Phase transfer of the complexed species.
- An experimental optimal dissolution pH value of 4.5 was determined for malonic acid, which represents an advantage for its use in replacement of oxalic acid.

5.2. Coupon tests

- Different methods were used to grow oxide films on several Ni Alloys. Their characterizations show that oxide composition and structure are similar to reported data.
- A two stage descaling method which reductive step includes malonic acid and Fe(II) (APMAL) gave similar results than APAC for oxides grown on Alloy 800 and 600 under simulated PHWR conditions. APMAL procedure was even better than APAC for Alloy 800 thick oxide removal.

These results demonstrate that malonic acid can be foreseen as a good potential reagent for decontaminating or chemical cleaning solutions to be applied on corroded stainless steels and other Ni-rich alloys. Nevertheless, more tests must be carried out in order to extrapolate these results to a practical use in, by instance, the nuclear industry.

Acknowledgements

Work supported by Comisión Nacional de Energía Atómica (CNEA) and Agencia Nacional de Promoción de Ciencia y Tecnología de Argentina (Project PICT 06-06631).

References

[1] R.L. Tapping, Y.C. Lu, M.D. Pandey, in: Proceedings of the 13th International Conference on Environmental Degradation of Materials in Nuclear Power Systems, Whistler, British Columbia, August19–23, 2007.
[2] R.L. Tapping, J. Nucl. Mater. 383 (2008) 1.
[3] R.L. Tapping, R.D. Davidson, E. McAlpine, D.H. Lister, Corros. Sci. 26 (1986) 563.
[4] "Decontamination of Water Cooled Reactors", IAEA Technical Reports Series N 365, Vienna, 1994.
[5] D.H. Lister, R.D. Davidson, E.Mc Alpine, Corros. Sci. 27 (1987) 113.
[6] M.G. Alvarez, A.M. Olmedo, M. Villegas, J. Nucl. Mater. 229 (1996) 93.
[7] A.J.G. Maroto, M.A. Blesa, M. Villegas, A.M. Olmedo, R. Bordoni, M.G. Alvarez, R. Sainz, in: Proceedings of the Third International Steam Generator and Heat Exchanger Conference, Toronto, published by Canadian Nuclear Soc., 1998, p. 409.
[8] A.M. Olmedo, R. Bordoni, in: Proceedings of CONAMET/SAM 2006, Sexto Congreso de Metalurgia, Santiago de Chile, Chile, 28 November–1 December, 2006 (Sess. Q).
[9] A.M. Olmedo, R. Bordoni, M. Miyagusuku, M. Chocrón, N. Fernández, D. Quinteros, L. Ovando, R. Sainz, in: Proceedings of VGB Water Conference, NPC 08, Berlin, Germany, 14–18 September 2008 (works 019 and 020).
[10] B. Stellwag, Corros. Sci. 40 (1998) 337.
[11] D.H. Lister, Nucl. Energy 32 (1993) 103.
[12] T. Terachi, N. Totsuka, T. Yamada, T. Nakagawa, H. Deguchi, M. Horiuchi, M. Oshitani, J. Nucl. Sci. Technol. 40 (2003) 509.
[13] S.E. Ziemniak, M. Hanson, Corros. Sci. 48 (2006) 498.
[14] J. Panter, B. Viguier, J.M. Cloué, M. Foucault, F. Combrade, E. Andrieu, J. Nucl. Mater. 348 (2006) 213.
[15] E.B. Borghi, S.P. Alí, P.J. Morando, M.A. Blesa, J. Nucl. Mater. 229 (1996) 115.
[16] J.A. Ayres, Decontamination of Reactors and Equipment, Ronald Press, New York, 1970.
[17] M.M. Osterhout, Decontamination and Decommissioning of Nuclear Facilities, Plenum Press, New York, 1980.
[18] K. Varga, P. Baradlai, G. Hirschberg, Z. Németh, D. Oravetz, J. Schunk, P. Tilky, Electrochim. Acta 46 (2001) 3783.
[19] K. Varga, Z. Nemeth, A. Szabó, K. Rodó, D. Oravetz, Z. Homonnay, J. Schunk, P. Telky, F. Korosi, J. Nucl. Mater. 348 (2006) 181.
[20] C.A. Figueroa, E.E. Sileo, P.J. Morando, M.A. Blesa, J. Colloid Interface Sci. 225 (2000) 403.
[21] C.A. Figueroa, E.E. Sileo, P.J. Morando, M.A. Blesa, J. Colloid Interface Sci. 244 (2001) 353.
[22] H. Tamura, E. Matijević, J. Colloid Interface Sci. 90 (1982) 1.
[23] E.E. Sileo, L. García Rodenas, C.O. Paiva-Santos, P. Stephens, P.J. Morando, M.A. Blesa, J. Solid State Chem. 179 (2006) 2237–2244.
[24] L.A. García Rodenas, M.A. Blesa, P.J. Morando, J. Solid State Chem. 181 (2008) 2350.
[25] D.L. Leussing, L. Newman, J. Am. Chem. Soc. 78 (1956) 552.
[26] D.H. Lister, E.Mc Alpine, W.H. Hocking, Corrosion Product Release in Light Water Reactors. EPRI-Rp. NP-3460, 1984.
[27] L.A. García Rodenas, P.J. Morando, M.A. Blesa, in: 11th International Conference on Surface and Colloid Science. Foz do Iguaçu, Brazil, September 2003.
[28] M.A. Blesa, P.J. Morando, A.E. Regazzoni, Chemical Dissolution of Metal Oxides, CRC Press, Boca Ratón, USA, 1994.
[29] M.G. Segal, R.M. Sellers, J. Chem. Soc. Faraday Trans. I 78 (1982) 1149.
[30] E.B. Borghi, P.J. Morando, M.A. Blesa, Langmuir 7 (1991) 1652.
[31] M.A. Blesa, A.J.G. Maroto, P.J. Morando, J. Chem. Soc. Faraday Trans. I 82 (1986) 2345.
[32] C.A. Figueroa, E.E. Sileo, P.J. Morando, M.A. Blesa, X Congreso Argentino de Investigación Fisicoquímica. Tucumán, Argentina, April 1997.
[33] D.H. Lister, Nucl. Sci. Eng. 58 (1975) 239.
[34] D.H. Lister, Nucl. Sci. Eng. 59 (1976) 406.
[35] O. Gautsch, F. Lanza, P. Weisgerber, Eur-Appl. Res. Rep. Nucl. Sci. Technol. Sect. 1 (1979) 125.
[36] D.W. Shoesmith, D.S. Mancey, D.C. Doern, M.G. Bailey, Corrosion 45 (1989) 149.
[37] l. Guinard, O. Kerrec, D. Noel, S. Gardey, F. Coulett, Nucl. Energy 36 (1997) 19.